

Optical Design of PICO, a Concept for a Space Mission to Probe Inflation and Cosmic Origins

Karl Young^{a†}, Marcelo Alvarez^b, Nicholas Battaglia^c, Jamie Bock^d, Jullian Borrill^e, David Chuss^f, Brendan Crill^g, Jacques Delabrouille^h, Mark Devlinⁱ, Laura Fissel^j, Raphael Flauger^k, Daniel Green^l, Kris Gorksi^g, Shaul Hanany^a, Richard Hills^m, Johannes Hubmayrⁿ, Bradley Johnson^o, Bill Jones^c, Lloyd Knox^p, Al Kogut^q, Charles Lawrence^g, Tomotake Matsumura^r, Jim McGuire^g, Jeff McMahon^s, Roger O’Brien^g, Clem Pryke^a, Brian M. Sutin^g, Xin Zhi Tan^a, Amy Trangsud^g, Qi Wen^a, and Gianfranco de Zotti^t

^aUniversity of Minnesota, USA

^bUniversity of California Berkeley, USA

^cPrinceton University, USA

^dCalifornia Institute of Technology, USA

^eLawrence Berkeley National Laboratory, USA

^fVillanova University, USA

^gJet Propulsion Laboratory, California Institute of Technology, USA

^hLaboratoire AstroParticule et Cosmologie and CEA/DAP, France

ⁱUniversity of Pennsylvania, USA

^jNational Radio Astronomy Observatory, USA

^kUniversity of California San Diego, USA

^lUniversity of Toronto, Canada

^mCavendish Laboratory, University of Cambridge, UK

ⁿNational Institute of Standards and Technology, USA

^oColumbia University, USA

^pUniversity of California Davis, USA

^qGoddard Space Flight Center, USA

^rKalvi IPMU, University of Tokyo, Japan

^sUniversity of Michigan, USA

^tOsservatorio Astronomico di Padova, Italy

ABSTRACT

The Probe of Inflation and Cosmic Origins (PICO) is a probe-class mission concept currently under study by NASA. PICO will probe the physics of the Big Bang and the energy scale of inflation, constrain the sum of neutrino masses, measure the growth of structure in the universe, and constrain its reionization history by making full sky maps of the cosmic microwave background with sensitivity 70 times higher than the Planck space mission. With bands at 21-799 GHz and arcmin resolution at the highest frequencies, PICO will make polarization maps of galactic synchrotron and dust emission to observe the role of Galactic magnetic fields in galactic evolution and star formation. We describe the current state of the PICO instrument design. We discuss the choice of optical system, present the design of the focal plane, and give the expected noise level.

did you review the abstract? does it accurately represent the contents of the paper? Is it highlighting the unique and new things you are reporting? Is it quantitative?

Keywords: Cosmic microwave background, cosmology, mm-wave optics, polarimetry, instrument design, satellite, mission concept

[†]E-mail: kyoung@astro.umn.edu, Telephone: 1 612 626 9149

1. INTRODUCTION

Currently, NASA funded spaces missions in astronomy and astrophysics are either Explorer missions with \$250M cost caps or flagship missions, such as JWST, which cost roughly \$3-\$5B. To study the science opportunities available at intermediate costs, NASA called for studies of ‘Probe’ class missions with \$1B cost caps. The Probe of Inflation and Cosmic Origins (PICO) is one of these NASA funded studies. This paper describes the status of the instrument optical design and focal plane approximately two thirds of the way through the study time line. The final PICO report will be sent to NASA at the end of 2018.

Astrophysical observations in the millimeter and sub-millimeter region of the electromagnetic spectrum contain a wealth of information about the formation, evolution, and structure of the Universe. The polarization and temperature anisotropies of the cosmic microwave background (CMB) encode fundamental physics information relating to the epoch of inflation, the mass of neutrinos, and the number of relic light particles in the early Universe. They also contain information about the formation of the first stars, galaxies, and clusters, as well as information on emission from the innermost regions of radio source jets. . Information about the role of magnetic fields in star formation and galactic evolution is obtainable by observing the polarized emission of Galactic dust, which traces magnetic fields, at high resolution. Targeting both of these regimes, PICO will survey the entire sky with unprecedented polarization sensitivity in 21 bands centered at 21–799 GHz. Details of these science targets and expected constraints from PICO are in a companion paper, Sutin et al.¹ In this paper we discuss the mission’s optical system, focal plane, and sensitivity.

2. SPACECRAFT AND MISSION

PICO will conduct scientific observations for five years from an orbit around the Earth-Sun L2 Lagrange point. The spacecraft design impacts the optical design and sensitivity in two primary ways; volume constraints limit the physical size of the telescope and optical component temperatures impact noise levels.

The maximum size of the spacecraft is limited by the launch vehicle, SpaceX’s Falcon 9, which carries payloads up to 4.6 m in diameter. This diameter limit sets the V-groove size which, along with the scan strategy, defines the ‘shadow cone’ in Figure 1. The shadow cone is the volume protected from solar illumination, and all optical components must remain within it. The shadow cone and inner V-grooves define an available volume for the telescope.

The temperatures of all optical elements are given in Figure 1. The optics box, secondary mirror, and focal plane are actively cooled, details of the thermal system are given in Sutin et al.¹

3. OPTICAL SYSTEM

The PICO telescope is a 1.4 m aperture modified open-Dragone. This choice was driven by a combination of science requirements and the physical limits discussed in Section 2. The science requirements are: a large diffraction limited field of view (DLFOV)* sufficient to support $\mathcal{O}(10^4)$ detectors, arcminute resolution at 800 GHz, low instrumental polarization, and low sidelobe response. Additionally, the transition edge sensor bolometers baselined for PICO require a telecentric focal plane which is sufficiently flat that it can be tiled by 10 cm detector wafers without reduction in optical quality.

More than 30 years ago Dragone analyzed the performance of several off-axis systems and found solutions with low cross-polarization at the center of the field of view and with astigmatism, or astigmatism and coma, canceled to first order.^{2–4} A number of recent CMB instruments used off-axis systems, and several began the design optimization with systems based on designs by Dragone.^{5–10} For PICO we begin the optimization with a Dragone system that to our knowledge has not been implemented in CMB instruments before. We call it an ‘open-Dragone’ because of its overall geometry and in contrast to the widely used ‘cross-Dragone’, see Figure 3.

We consider two additional Dragone systems, a Gregorian Dragone and a cross-Dragone, and compare the relative performance of all three systems in terms of DLFOV, compactness, and rejection of sidelobes. Compared to the open-Dragone, the Gregorian has half the DLFOV for the same F -number and cannot support $\mathcal{O}(10^4)$

* We consider an area in the FOV diffraction limited when the Strehl ratio is larger than 0.8.

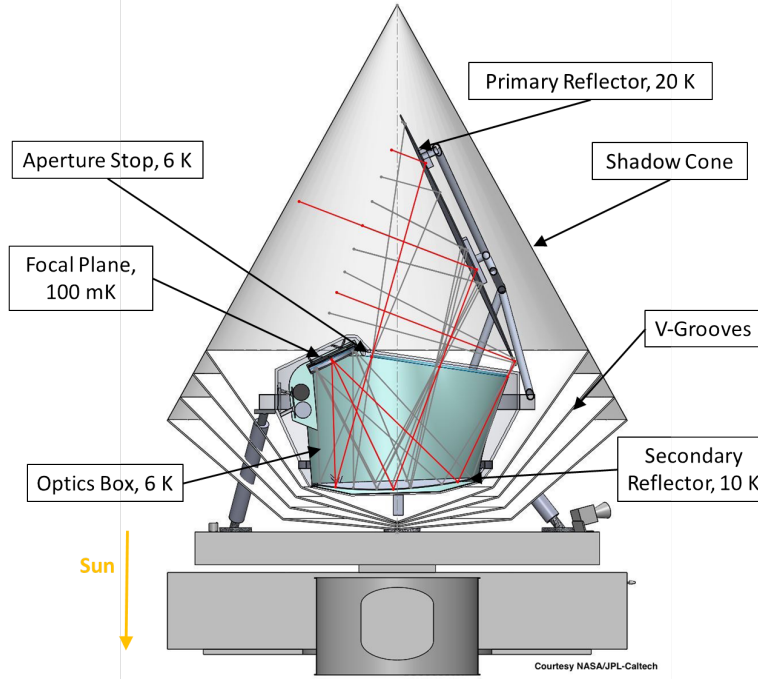


Figure 1. Mechanical design of the PICO satellite. Components relevant to this paper are labeled, for other details see Sutin et al.¹ The symmetry axis of the satellite precesses around the satellite-sun axis (orange arrow) with an angle of 26 deg. This precession defines the shadow cone which is shown in light gray.

detectors. It is therefore rejected. The cross-Dragone has roughly $4\times$ the DLFOV of the open-Dragone, but is more difficult to pack inside the spacecraft volume while avoiding the known sidelobes shown in Figure 2. We find the largest cross-Dragone which meets the PICO volume constraints has a 1.2 m aperture and an F -number of 2.5, while the largest open-Dragone aperture is 1.4 m with an F -number of 1.42. The larger F -number of the cross-Dragone system implies a larger physical focal plane, and therefore higher mass and cost, for the same number of pixels. For the PICO case, we conclude that the advantages of a low F -number and easily baffled sidelobes make the open-Dragone a good starting point for further optimization.

We design the initial open Dragone following Granet’s method.¹¹ We find a solution with low F -number, $F = 1.42$, the largest aperture that satisfies the volume constraints, and a large DLFOV. We force a circular aperture stop between the primary and secondary mirrors and numerically optimize its angle and position to obtain the best optical performance. The stop diameter provides an effective 1.4 m aperture on the primary for the center feed. Adding a stop in this way increases the size of the primary mirror, because the primary is unevenly illuminated at various field angles. Actively cooling the aperture stop, however, reduces detector noise, and the stop shields the focal plane from stray radiation. At this stage the system still meets the Dragone condition and is defined by the ‘Initial Open-Dragone’ parameters in Table 1.

In his publications Dragone provides a prescription to eliminate coma in addition to the cancellation of astigmatism in the baseline designs.³ The reflector corrections involve adding distortions to the primary and secondary reflectors which are proportional to r^4 where $r = 0$ is at the chief ray impact point on each mirror. We thus attempt to increase the DLFOV using two methods.

In the first method, one of the coauthors (RH) used Zemax to add Zernike polynomials to the base conics which describe the mirrors. These Zernike polynomials are offset from the symmetry axis of the conic by 624.2 cm for the primary and 76.1 cm for the secondary. This places the origin of polynomials at the chief ray impact point for each mirror. Inspired by the Dragone corrections, all Zernike terms up to fourth order and the first fifth order term are allowed to vary. The optimization metric is minimization of the rms spot diameter at the following locations: the center of the FOV, ± 2 deg in Y, and ± 4 deg in X. The center of the FOV is given a weight of 100

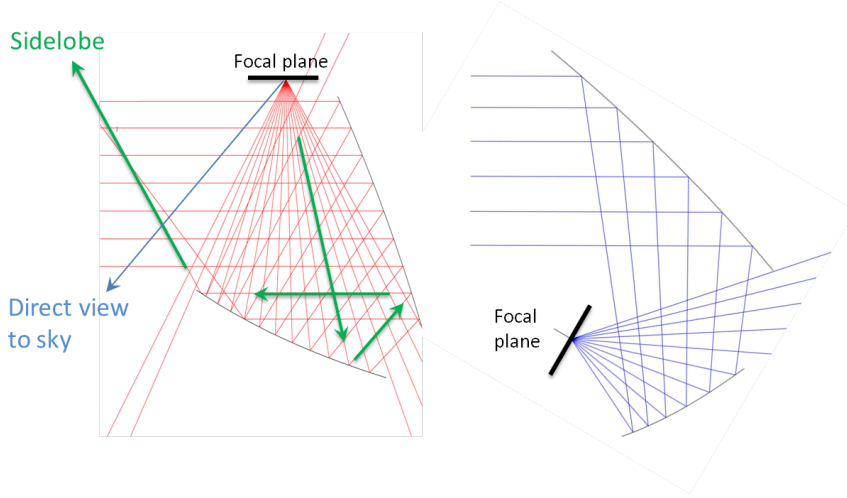


Figure 2. Comparison of sidelobes for a cross-Dragone (left) and an open-Dragone (right). Rays are traced from the center of the focal plane toward the sky. For both systems spillover around the secondary is straightforward to mitigate with absorptive baffles. However, the sidelobe and direct sky view in the cross-Dragone system require a long forebaffle or large F -number to mitigate, both of which are problematic in the PICO case.

while each outer point is given a weight of 1. To constrain the optimization, the X and Y effective focal lengths are held fixed as is the impact point of the chief ray on the focal plane. This optimization step increases the DLFOV by factors of 1.15, 2.4 and 10.5 at 21, 155 and 799 GHz, respectively. We improve the DLFOV at all frequencies by approximately 50% by rerunning the optimization and including a curved focal surface. A small ($\sim 4\%$) additional gain in DLFOV is achieved by adding Zernike terms up to sixth order, allowing the secondary to focal surface distance to vary, adding a weighted constraint on the effective focal length, and adding fields with weight of 0.01 to the rms spot diameter metric at ± 7.5 deg in Y and $+15$ deg in X. These additional fields are necessary to constrain the corrections at the mirror edges.

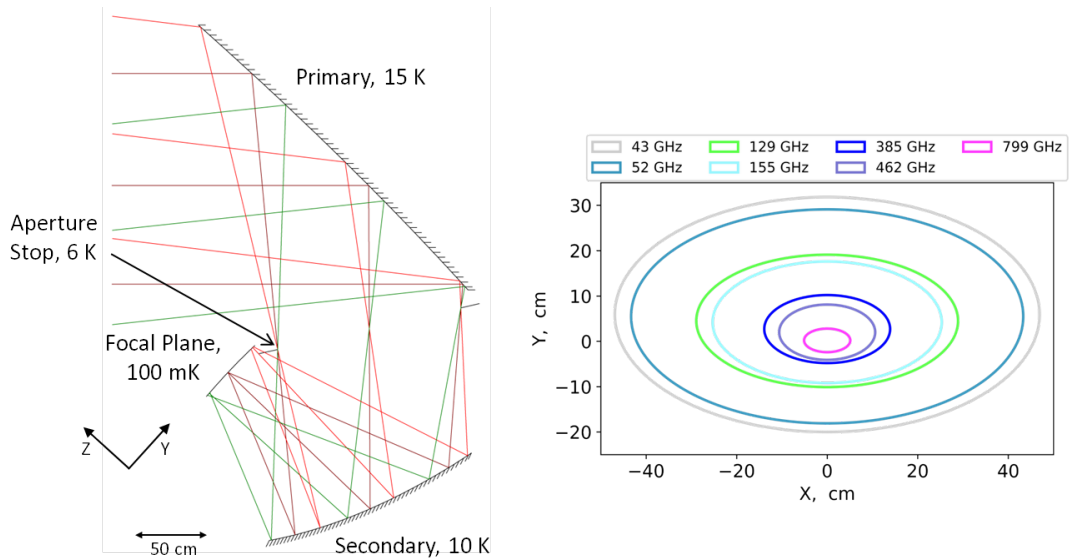


Figure 3. Raytrace (left) and Strehl = 0.8 contours (right) for the PICO optical design.

In the second optimization method, another coauthor (JM) uses CodeV and allows more of the geometric

Table 1. Telescope geometric parameters

PICO optical system					Initial Open-Dragone ^b	
	Primary	Secondary	Telescope parameters ^b		Fundamental design parameters	
Mirror size ^a (cm)	270 × 205	160 × 158	Aperture (cm)	140	Aperture (cm)	140
Radius of curvature (cm)	∞	136.6	F -number	1.42	θ_0 (deg)	90
Conic constant, k	0	-0.926	h (cm)	624.2	θ_e (deg)	20
Normalization radius (cm)	524.8	194.1	α (deg)	74.2	θ_p (deg)	140
4th Zernike Coefficient (cm)	2018.4	-61.1	β (deg)	62.3	L_m (cm)	240
9th Zernike Coefficient (cm)	-37.0	16.7	L_m (cm)	229.3	Derived parameters	
10th Zernike Coefficient (cm)	-2919.8	-15.1	L_s (cm)	140.5		
11th Zernike Coefficient (cm)	-1292.7	22.3	Focal Surface		F -number	1.42
12th Zernike Coefficient (cm)	120.6	-3.8			h (cm)	624.2
13th Zernike Coefficient (cm)	-74.5	4.9	Ellipse major axes (cm)	69 x 45	α (deg)	38.6
19th Zernike Coefficient (cm)	-75.8	3.4	Ellipse major axes (deg)	19 x 13	β (deg)	101.4
20th Zernike Coefficient (cm)	-398.9	6.3	Radius of curvature (cm)	455	L_s (cm)	122.2
21st Zernike Coefficient (cm)	-319.5	23.3			Primary, f (cm)	312.1
22nd Zernike Coefficient (cm)	-276.6	-8.5			Secondary, a (cm)	131
23rd Zernike Coefficient (cm)	-201.6	-3.2			Secondary, e	1.802
24th Zernike Coefficient (cm)	-127.4	-1.9				
25th Zernike Coefficient (cm)	-55.0	0.1				

^a The maximum physical size of the mirrors.

^b Telescope parameters follow the definitions in Granet 2001.¹¹

parameters of the system to vary. To adjust the mirror shapes, we add Zernike polynomial corrections to the conic surfaces which define the two mirrors. The Zernike polynomials are defined on the same coordinates as the base conics. We vary the 4th and 9th-13th terms of the Zernike polynomials. We allow the focal surface curvature and focal surface to secondary distance L_s to vary. The primary-secondary distance L_m , primary offset h , and the primary and secondary rotation angles, α and β , are varied as well. The optimization metric is the rms spot diameter across the field of view, with weighted constraints requiring telecentricity and maintaining the X- and Y-focal lengths. We add Lagrange constraints to enforce beam clearances and place an upper limit on overall system size. Once the optimization converges to an acceptable optical system, we add higher order Zernike terms, 19th-25th, and refine the mirror shapes using the same metric and constraints. The current PICO optical design is from this optimization procedure.

Figure 4 shows that the second optimization method greatly increases the DLFOV relative to the initial open-Dragone design. The DLFOV is increased by factors of 1.9, 3.8, 4.3, and 4.6 at 21, 129, 155, and 799 GHz, respectively. The most important gain is at 129 and 155 GHz where the extra area allows us to add many more ‘C’ and ‘D’ pixels, see Figure 5 and Section 4, which contain the bands most sensitive to the CMB. Being able to pack 100’s of ‘C’ and ‘D’ pixels into the focal plane is what allows PICO to reach unprecedented levels of CMB sensitivity. Compared to the first optimization method, the second gives somewhat better performance at the lower frequencies, with 1.11 and 1.15 times large DLFOV at 21 and 155 GHz, respectively. Method two gives a smaller DLFOV at 799 GHz, only 0.3 times the method one area, but the DLFOV is still sufficient for the number of 799 GHz detectors we require. Figure 4 also shows the second optimization method reduces the overall telescope volume, allowing it to fit more easily within the shadow cone.

do you mean if we had only optimization method 1 we wouldn’t reach our goals? not really, because the goals are poorly defined. But total CMB sensitivity would be lower with method 1 only.

The geometric parameters of the PICO optical system are given in Table 1. The system is diffraction limited for 799 GHz at the center of the field of view. At 155 GHz the DLFOV is 82.4 deg² and the total throughput for all frequencies is 910 cm²sr. Figure 3 shows Strehl of 0.8 contours for all pixel types. The slightly concave focal surface, which has a radius of curvature of 4.55 m, is telecentric to within 0.12 deg across the entire FOV.

An additional benefit of the optimization is the concave focal surface. The open-Dragone’s focal surface is naturally curved. Matching this curvature reduces defocus and increases the DLFOV as well as increasing telecentricity. The unoptimized system is telecentric to within 2.5 deg while the optimized version is telecentric

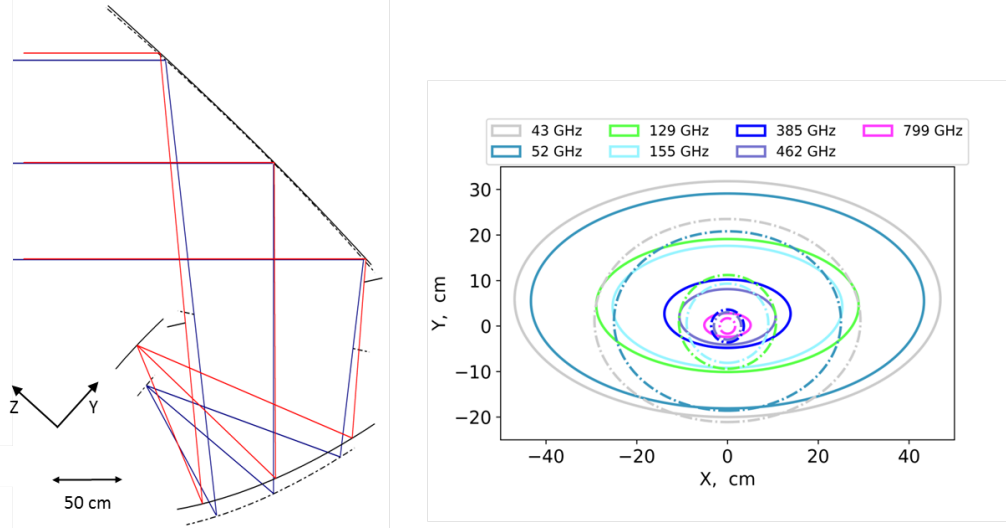


Figure 4. Comparison between the open-Dragone optimized using method two and the initial open-Dragone. The ray traces (left) are aligned at the chief ray impact point on the primary. The optimized system (red rays, solid mirrors) is smaller in the vertical direction than the unoptimized version (blue rays, dash-dot mirrors). The overlaid Strehl = 0.8 contours (right) show the improvement at all frequencies in the optimized (solid lines) system over the unoptimized (dash-dot lines) system.

to within 0.12 deg. If the focal surface is too strongly curved tiling it with flat detector wafers would result in large defocus at the edges of these wafers. This is not the case for PICO. The focal surface radius of curvature, 4.55 m, results in a defocus of 0.1 mm for the edge of a 10 cm wafer.

4. FOCAL PLANE

Modern mm/sub-mm detectors are photon noise limited, therefore the primary way to increase sensitivity is to increase the number of detectors. The PICO focal plane has 12,996 detectors, 175 times the number flown on *Planck*. PICO achieves this by having a large DLFOV and using multichroic pixels (MCPs).^{12,13} The MCP architecture assumed for PICO has three bands per pixel with two single polarization transition edge sensor (TES) bolometers per band and therefore six bolometers per pixel. We assume the MCPs are coupled to free space using lenslets and sinuous antennae,¹² however the pixel size, number, and spacing is relatively agnostic to the coupling scheme meaning the current layout would not change significantly if horn or phased array coupling was used instead.

PICO has 21 overlapping bands with centers spanning the range 21–799 GHz. The bands are divided amongst nine pixel types, A-I; see Figure 5. The 25% fractional bandwidth is broader than the interband spacing causing neighboring bands to overlap and requiring them to be in separate pixels. The exceptions to the MCP architecture are the highest three bands, because they are above the superconducting band gap of niobium which is used for the transmission lines, antennae, and filters of the MCPs. For bands G, H, and I, we will use feedhorn-coupled polarization sensitive bolometers similar to those used with *Planck*¹⁴ and Herschel SPIRE.¹⁵

Figure 6 shows the PICO focal plane. We optimize the diameter of each MCP by calculating the array sensitivity for that pixel type. The calculation includes the increased illumination of the aperture stop as the pixel diameter decreases, as described in Section 5.1. We choose a pixel diameter of $2.1F\lambda_{\text{mid}}$, where λ_{mid} refers to the center band of each pixel. This gives an edge taper, T_e , on the stop of 10 dB for the center band of each pixel.

SH Stopped Here

The polarization sensitive bolometers in each MCP are oriented perpendicular to each other. Differencing the bolometers allows each pixel to measure Stokes Q or, if the pixel is rotated by 45 deg, Stokes U. This Q/U

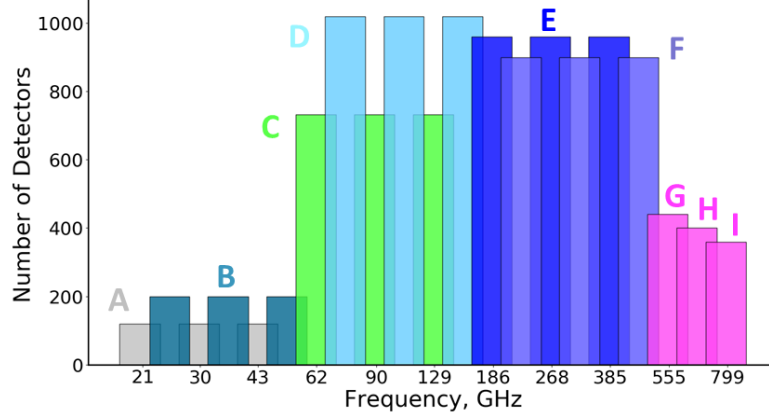


Figure 5. Frequency coverage of the PICO bands. Each color (excluding magenta) denotes a different MCP, labeled A-F. The bar height indicates the number of detectors per band. Bar width gives the bandwidth. All bands are top-hats with 25% fractional bandwidth; the x -axis is logarithmic. The three highest frequencies (magenta) are the single color pixels G, H, and I.

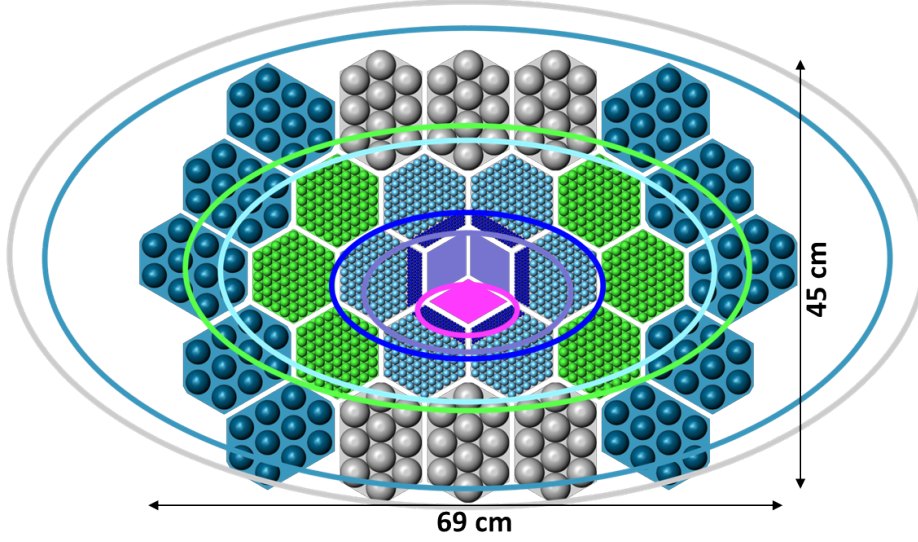


Figure 6. PICO focal plane layout with Strehl = 0.8 contours for each pixel type. The pixel and Strehl contour colors match the band colors, A-I, in Figure 5

measurement is in the instrument reference frame with the x -axis parallel to the scan direction. We rotate neighboring pixels which scan over the same sky location by 45 deg, as shown in Figure 7. This layout reduces systematic errors by maximizing the number of Q,U pixel pairs which have almost identical optical paths and measure sky locations as close to simultaneously as possible.

Two multiplexing methods, time domain (TDM) and frequency domain (FDM), were explored for PICO. Trade-off details are discussed in Sutin et al.¹ The current PICO baseline is TDM, but the choice is not a driver for the focal plane layout or noise discussed in this paper.

5. INSTRUMENT NOISE

We develop an end to end white noise model of the PICO instrument to predict full mission sensitivity and provide a metric by which to evaluate optical, mechanical, and mission design trade-offs. This model does not include

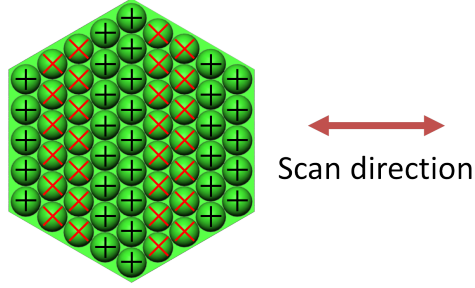


Figure 7. Layout of pixels sensitive to Stokes Q (black crosses) and Stokes U (red exes) for an example wafer.

1/f noise or estimates of possible systematic effects. To construct the model we follow the standard process^{16,17} of estimating the optical load, calculating properties of the TES bolometers, calculating noise equivalent power (NEP) by source, combining all NEP terms to get detector noise, and finally combining all detectors to get full mission sensitivity. Each of these steps includes various assumptions and design decisions, which are discussed in this section. The assumptions are summarized in Table 2.

Table 2. Noise model assumptions, see text for details.

Throughput	single moded, λ^2
Fractional Bandwidth	25%
Mirror emissivity	$\epsilon = \epsilon_0 \sqrt{\nu/150 \text{ GHz}}, \epsilon_0 = 0.07\%$
Aperture stop emissivity	1
Low pass filter reflection loss	8%
Low pass filter absorption loss ^a	frequency dependent, 0.2%–2.8%
Bolometer absorption efficiency	70%
T_e , middle band in pixel (dB)	10
Bose noise fraction, ξ	1
Bolometer yield	100% Change to 90%
Bath temperature, T_o (mK)	100
TES critical temperature, T_c (mK)	187
Safety factor, $P_{\text{sat}}/P_{\text{abs}}$	2
Thermal power law index, n	2
Intrinsic SQUID noise ($\text{aW}/\sqrt{\text{Hz}}$)	3
TES operating resistance, Ω	0.03
TES transition slope, α	100
TES loop gain	14
Mission length (years)	5
Observing efficiency	95%

^aAssumes separate metal mesh in polypropylene filters for each wafer.

5.1 Single bolometer noise

5.1.1 Model

The sources of optical load are the CMB, primary and secondary mirrors, aperture stop, and a low pass optical filter. These elements are shown schematically in Figure 8. The total load absorbed at the bolometer is the sum of the power emitted by each element reduced by the transmission efficiency of the elements between the emitting surface and the bolometer. The absorbed power is,

$$P_{\text{abs}} = (((P_{\text{CMB}}\eta_{\text{PRI}} + P_{\text{PRI}})\eta_{\text{stop}} + P_{\text{stop}}(1 - \eta_{\text{stop}}))\eta_{\text{SEC}} + P_{\text{SEC}})\eta_{\text{filter}} + P_{\text{filter}})\eta_{\text{bolo}}, \quad (1)$$

where P_{elem} is the in band power emitted by a given element for a single polarization and η_{elem} is the efficiency of the element. Power emitted by the stop is a special case. We multiply P_{stop} by $(1 - \eta_{\text{stop}})$ because η_{stop}

is spillover efficiency, the fraction of the throughput which passes through the stop, therefore $(1 - \eta_{\text{stop}})$ is the fraction of the throughput which views the stop.

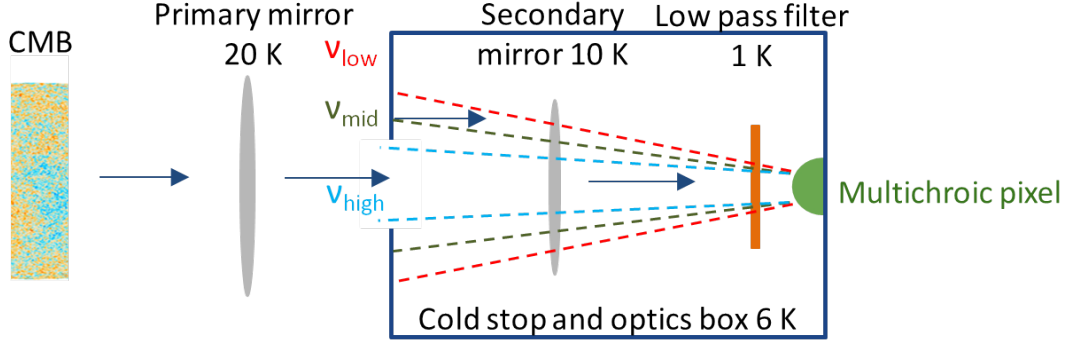


Figure 8. Schematic representation of the prediction of optical load. Power emitted by each element is modified by the efficiency of the following elements and added to the total expected load. The multichroic pixel illuminates the stop differently for each of the three bands.

For PICO, the CMB and stop dominate the optical loading as shown in Figure 9. The jumps in load between neighboring bands, seen in Figure 9 around 70 and 200 GHz, are due to η_{stop} changing with frequency which is a consequence of using MCPs. The MCP angular beam width is dependent on the wavelength and pixel diameter as,¹⁶

$$\theta_{1/e^2} = \frac{2.95\lambda}{\pi D_{\text{px}}} \quad (2)$$

The edge taper, T_e , of the middle frequency band in each pixel is chosen to be 10 dB. For the upper and lower bands T_e is calculated using Equation 2. This changing illumination of the stop is shown schematically by the dashed rays in Figure 8. For each MCP, A-H, T_e is 4.8, 10, and 20.7 dB for the lower, middle, and upper bands, respectively. These edge tapers correspond to η_{stop} of 0.68, 0.90, and 0.99. The changing η_{stop} has three main effects; uneven optical load between bands, varying NEP to noise equivalent temperature (NET) conversion between bands, and telescope beam size not scaling smoothly with λ .

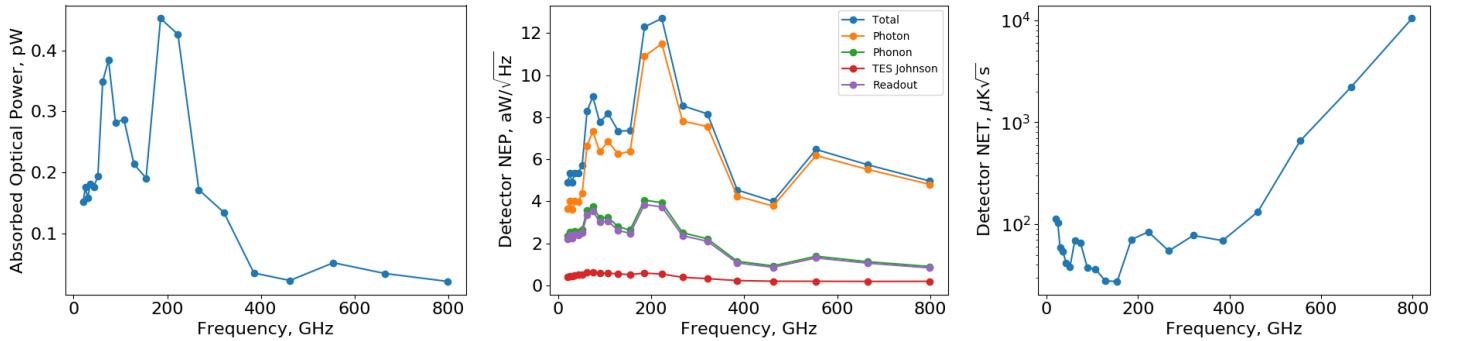


Figure 9. Left: Expected optical loads for single polarization PICO bolometers. Center: Breakdown of NEP across the PICO frequency range. Photon noise dominates even at the lowest frequencies. Right: Single detector NET, temperature sensitivity, across the PICO bands.

We consider four noise sources per bolometer; photon, phonon, TES Johnson, and readout. Photon noise

depends on the absorbed power,¹⁸

$$NEP_\gamma^2 = \int_{\text{band}} 2h\nu p_\nu d\nu + 2\xi \int_{\text{band}} p_\nu^2 d\nu, \quad (3)$$

where p_ν is the power spectral density for a single polarization absorbed at the bolometer and $\xi = 1$ is the fraction of correlated Bose photon noise. The factor of 2 in the Bose noise term is because we use single polarization bolometers. From P_{abs} we calculate the TES bolometer properties and phonon noise.¹⁹ The last noise term intrinsic to the bolometer is the TES Johnson noise. All noise sources in the cold and warm readout electronics are lumped under the readout term. The NEP for each noise source is shown in Figure 9.

5.1.2 Results

For PICO, photon noise dominates at all frequencies as shown in Figure 9. Bose noise is most significant at lower frequencies with $NEP_{\text{Bose}}/NEP_{\text{Poisson}} = 1.5$ in the lowest band. However, since Poisson noise increases as $\sqrt{\nu}$ it equals Bose noise at 30 GHz and dominates at higher bands; $NEP_{\text{Bose}}/NEP_{\text{Poisson}} < 10\%$ at 321 GHz. Phonon noise is the second most significant source, $NEP_{\text{phonon}}/NEP_{\text{photon}}$ ranges from 65% at 21 GHz to 19% at 799 GHz.

For TDM readout, phonon and readout noise are roughly equal with TES Johnson noise being insignificant. We also modeled FDM readout. For FDM the TES Johnson noise is higher, 2/3 of the readout NEP, but the readout noise is lower. Comparing the combined TES Johnson and readout NEPs for TDM and FDM we find essentially identical performance with total noise differing by less than 3% across all bands. For both systems we require a focal plane temperature, T_o , of 100 mK and a bolometer safety factor of 2 to remain photon noise dominated at the lowest bands.

The primary driver of noise levels is the optical load. The combination of the CMB and aperture stop make up the majority of the load in all bands. The load from the mirrors is greatest at 799 GHz where it is 90% of that from the CMB and stop. The CMB provides more than half the load in the middle and upper bands of the multichroic pixels, but the stop dominates the load in the lowest band of each pixel. Load from the stop in the lowest band of each pixel ranges from 1.2 times the CMB load at 21 GHz to a maximum of 4.7 times the CMB load at 223 GHz.

5.2 Combined array noise

Using single detector NEPs from Section 5.1 and the detector counts from Section 4 we calculate the combined NEP of the detector array for each band. Combining detectors simply reduces noise by \sqrt{N} except for Bose photon noise. For the lowest band of each MCP the pixels over sample the PSF, pixel spacing is $0.4F\lambda$, resulting in correlated Bose noise between pixels. Accounting for this effect gives a 26% increase in the combined array NEP of the lowest band, 21 GHz, and a 0.003% increase in array NEP at the highest band, 799 GHz.

From the array NEP we convert to NET per band,

$$\frac{NEP}{NET} = \sqrt{2}\eta_{\text{opt}} \int_{\text{band}} \frac{dp_\nu}{dT} \Big|_{T_{\text{CMB}}} d\nu. \quad (4)$$

The η_{opt} term contributes to the ‘jumps’ in NET seen in Figure 9, because η_{opt} varies band to band.

All the above calculations are for sensitivity to temperature and are given in Table 3. Assuming evenly weighted observations of the full sky and 5 years observing at 95% efficiency, we calculate full mission map sensitivities in polarization; final column in Table 3. Combining all bands gives a total CMB map depth for the entire PICO mission of $0.62 \mu\text{K}_{\text{CMB-arcmin}}$.

6. CONCLUSIONS/SUMMARY

The PICO optical system is a simple two mirror open-Dragone which we numerically optimize to maximize the DLFOV. The addition of a cold aperture stop and cold mirrors minimize optical load and reduce noise. The focal plane takes advantage of the large DLFOV and MCP technology to implement 12996 polarization sensitive detectors in 21 bands from 21-799 GHz. When combining all bands, our instrument noise model predicts full mission polarization map depth of $0.62 \mu\text{K}_{\text{CMB-arcmin}}$.

Table 3. PICO frequency channels and noise.

Pixel Type	Band GHz	FWHM arcmin	Bolometer NEP aW/\sqrt{Hz}	Bolometer NET $\mu\text{K}_{\text{CMB}}\sqrt{s}$	N_{bolo}	Array NET $\mu\text{K}_{\text{CMB}}\sqrt{s}$	Polarization map depth $\mu\text{K}_{\text{CMB}}\text{-arcmin}$	Jy/sr
A	21	38.4	4.89	112.2	120	12.9	18.2	XX
B	25	32.0	5.33	103.0	200	9.07	12.8	XX
A	30	28.3	4.92	59.4	120	5.60	7.88	XX
B	36	23.6	5.36	54.4	200	3.96	5.58	XX
A	43	22.2	5.33	41.7	120	3.80	5.36	XX
B	52	18.4	5.73	38.4	200	2.71	3.82	XX
C	62	12.8	8.29	69.2	732	2.97	4.19	XX
D	75	10.7	8.98	65.4	1020	2.34	3.29	XX
C	90	9.5	7.76	37.7	732	1.41	1.99	XX
D	108	7.9	8.18	36.2	1020	1.15	1.61	XX
C	129	7.4	7.35	27.8	732	1.03	1.45	XX
D	155	6.2	7.36	27.5	1020	0.86	1.21	XX
E	186	4.3	12.30	70.8	960	2.39	3.36	XX
F	223	3.6	12.70	84.2	900	2.89	4.07	XX
E	268	3.2	8.55	54.8	960	1.77	2.49	XX
F	321	2.6	8.16	77.6	900	2.59	3.64	XX
E	385	2.5	4.54	69.1	960	2.23	3.14	XX
F	462	2.1	4.00	132.6	900	4.42	6.22	XX
G	555	1.5	6.47	657.8	440	31.4	44.1	XX
H	666	1.3	5.74	2212	400	111	156	XX
I	799	1.1	4.97	10430	360	550	774	XX
Total					12996	0.44	0.62	

7. ACKNOWLEDGMENTS

This Probe mission concept study is funded by NASA grant #NNX17AK52G. Gianfranco de Zotti acknowledges financial support from the ASI/University of Roma–Tor Vergata agreement n. 2016-24-H.0 for study activities of the Italian cosmology community. Jacques Delabrouille acknowledges financial support from PNCG for participating to the PICO study.

REFERENCES

- [1] Sutin, B. M., Alvarez, M., Battaglia, N., et al., “PICO - the probe of inflation and cosmic origins,” *Proc. SPIE* **10698** (2018).
- [2] Dragone, C., “Offset multireflector antennas with perfect pattern symmetry and polarization discrimination,” *Bell Labs Technical Journal* **57**(7), 2663–2684 (1978).
- [3] Dragone, C., “First-order correction of aberrations in Cassegrainian and Gregorian antennas,” *IEEE Transactions on Antennas and Propagation* **31**, 764–775 (September 1983).
- [4] Dragone, C., “Unique reflector arrangement with very wide field of view for multibeam antennas,” *Electronics Letters* **19**(25), 1061–1062 (1983).
- [5] Fargant, G., Dubruel, D., Cornut, M., et al., “Very wide band telescope for Planck using optical and radio frequency techniques,” in *[UV, Optical, and IR Space Telescopes and Instruments]*, Breckinridge, J. B. and Jakobsen, P., eds., *Proc. SPIE* **4013**, 69–79 (July 2000).
- [6] Swetz, D. S., Ade, P. A. R., Amiri, M., et al., “Overview of the Atacama Cosmology Telescope: Receiver, Instrumentation, and Telescope Systems,” *ApJS* **194**, 41 (June 2011).
- [7] Padin, S., Staniszewski, Z., Keisler, R., et al., “South Pole Telescope optics,” *Appl. Opt.* **47**, 4418–4428 (Aug. 2008).
- [8] de Bernardis, P., Ade, P. A. R., Baselmans, J. J. A., et al., “Exploring cosmic origins with CORE: The instrument,” *Journal of Cosmology and Astro-Particle Physics* **2018**, 015 (Apr. 2018).

- [9] Matsumura, T., Akiba, Y., Arnold, K., et al., “LiteBIRD: Mission Overview and Focal Plane Layout,” Journal of Low Temperature Physics **184**, 824–831 (Aug. 2016).
- [10] Parshley, S., Niemack, M., and Hills, R. E., “The optical design of the six-meter CCAT-prime and Simons Observatory telescopes,” Proc. SPIE **10700** (2018).
- [11] Granet, C., “Designing classical Dragonian offset dual-reflector antennas from combinations of prescribed geometric parameters,” IEEE Antennas and Propagation Magazine **43**, 100–107 (Dec. 2001).
- [12] Suzuki, A., Arnold, K., Edwards, J., et al., “Multi-chroic dual-polarization bolometric detectors for studies of the cosmic microwave background,” Journal of Low Temperature Physics **176**, 650–656 (Sep 2014).
- [13] Datta, R., Hubmayr, J., Munson, C., et al., “Horn Coupled Multichroic Polarimeters for the Atacama Cosmology Telescope Polarization Experiment,” Journal of Low Temperature Physics **176**, 670–676 (Sept. 2014).
- [14] Lamarre, J. M., Puget, J. L., Ade, P. A. R., et al., “Planck pre-launch status: The HFI instrument, from specification to actual performance,” A&A **520**, A9 (Sept. 2010).
- [15] Griffin, M. J., Abergel, A., Abreu, A., et al., “The Herschel-SPIRE instrument and its in-flight performance,” A&A **518**, L3 (July 2010).
- [16] Suzuki, A., Multichroic Bolometric Detector Architecture for Cosmic Microwave Background Polarimetry Experiments, PhD thesis, University of California, Berkeley (Jan. 2013).
- [17] Aubin, F., Detector Readout Electronics for EBEX: A Balloon-borne Cosmic Microwave Background Polarimeter, PhD thesis, McGill University (2013).
- [18] Richards, P. L., “Bolometers for infrared and millimeter waves,” Journal of Applied Physics **76**, 1–24 (July 1994).
- [19] Mather, J. C., “Bolometer noise: nonequilibrium theory,” Appl. Opt. **21**, 1125–1129 (Mar. 1982).